



Early JWST Imaging Reveals Strong Optical and NIR Color Gradients in Galaxies at $z \sim 2$ Driven Mostly by Dust

Tim B. Miller¹ , Katherine E. Whitaker^{2,3} , Erica J. Nelson⁴ , Pieter van Dokkum¹ , Rachel Bezanson⁵ , Gabriel Brammer³ , Kasper E. Heintz³ , Joel Leja^{6,7,8} , Katherine A. Suess^{9,10} , and John R. Weaver²

¹ Department of Astronomy, Yale University, 52 Hillhouse Avenue, New Haven, CT 06511, USA; tim.miller@yale.edu

² Department of Astronomy, University of Massachusetts, Amherst, MA 01003, USA

³ Cosmic Dawn Center (DAWN), Niels Bohr Institute, University of Copenhagen, Jagtvej 128, KØbenhavn N, DK-2200, Denmark

⁴ Department for Astrophysical and Planetary Science, University of Colorado, Boulder, CO 80309, USA

⁵ Department of Physics and Astronomy and PITT PACC, University of Pittsburgh, Pittsburgh, PA 15260, USA

⁶ Department of Astronomy & Astrophysics, The Pennsylvania State University, University Park, PA 16802, USA

⁷ Institute for Computation & Data Sciences, The Pennsylvania State University, University Park, PA 16802, USA

⁸ Institute for Gravitation and the Cosmos, The Pennsylvania State University, University Park, PA 16802, USA

⁹ Department of Astronomy and Astrophysics, University of California, Santa Cruz, 1156 High Street, Santa Cruz, CA 95064 USA

¹⁰ Kavli Institute for Particle Astrophysics and Cosmology and Department of Physics, Stanford University, Stanford, CA 94305, USA

Received 2022 September 26; revised 2022 November 18; accepted 2022 November 28; published 2022 December 23

Abstract

Recent studies have shown that galaxies at cosmic noon are redder in the center and bluer in the outskirts, mirroring results in the local universe. These color gradients could be caused by gradients in either the stellar age or dust opacity; however, distinguishing between these two causes is impossible with rest-frame optical photometry alone. Here we investigate the underlying causes of the gradients from spatially resolved rest-frame $U - V$ versus $V - J$ color-color diagrams measured from early observations with the James Webb Space Telescope. We use 1–4 μm NIRCcam photometry from the CEERS survey of a sample of 54 galaxies with $\log M_*/M_\odot > 10$ at redshifts $1.7 < z < 2.3$ selected from the 3D-HST catalog. We model the light profiles in the F115W, F200W, and F356W NIRCcam bands using *imcascade*, a Bayesian implementation of the multi-Gaussian expansion technique that flexibly represents galaxy profiles using a series of Gaussians. We construct resolved rest-frame $U - V$ and $V - J$ color profiles. The majority of star-forming galaxies have negative gradients (i.e., redder in the center, bluer in the outskirts) in both $U - V$ and $V - J$ colors consistent with radially decreasing dust attenuation. A smaller population (roughly 15%) of star-forming galaxies have positive $U - V$ but negative $V - J$ gradients implying centrally concentrated star formation. For quiescent galaxies, we find a diversity of UVJ color profiles, with roughly one-third showing star formation in their center. This study showcases the potential of JWST to study the resolved stellar populations of galaxies at cosmic noon.

Unified Astronomy Thesaurus concepts: [Galaxy structure \(622\)](#); [High-redshift galaxies \(734\)](#); [Galaxy colors \(586\)](#)

1. Introduction

Measuring and modeling the colors of stellar populations provides great insight into their physical nature. In the local universe, galaxies are known to have gradients in their radial color profile, indicating complex multicomponent formation histories. Observed in the local universe since the late 1980s (Kormendy & Djorgovski 1989; Franx & Illingworth 1990), both star-forming and quiescent galaxies (or late and early types) display negative color gradients (i.e., redder in the center, bluer in the outskirts). In star-forming galaxies, like the Milky Way, this is usually due to multiple stellar populations, i.e., an old red bulge and a young blue disk. In quiescent, or early-type, galaxies, the cause is thought to be lower metallicity in the outskirts (Wu et al. 2005; Tortora et al. 2011) with the additional possibility of an age gradient (La Barbera & de Carvalho 2009).

Recent studies have found similar results at $z > 1$, with negative optical color gradients in all types of galaxies. These gradients have been observed either directly (Wuyts et al. 2012; Szomoru et al. 2013; Liu et al. 2016, 2017; Wang et al. 2017;

Miller et al. 2022) or implicitly through comparing mass-weighted radii to light-weighted radii (Chan et al. 2016; Suess et al. 2019; Mosleh et al. 2020). Mass-to-light ratio is correlated with optical color, so the fact that mass-weighted radii are smaller than light-weighted radii also implies negative color gradients. At $z > 1$, spaced-based imaging is needed to resolve the structure of galaxies. Until very recently, these studies relied on Hubble Space Telescope (HST) imaging, but it is limited by its longest observable wavelength of 1.6 μm , which traces the rest-frame optical at $z > 1$.

A limitation imposed by the lack of high-resolution IR imaging is the inability to understand the causes of these color gradients. Star formation history, dust attenuation, and, to a lesser extent, metallicity and nebular emission lines all contribute to the optical colors of galaxies producing degeneracies between these parameters when interpreting optical colors alone. Longer-wavelength measurements, especially in the near-infrared (NIR), are often used to break these degeneracies. In particular, the plane of rest-frame $U - V$ and $V - J$ colors, the UVJ diagram, is commonly used (Labbé et al. 2005; Wuyts et al. 2007). In this plane, the effects of dust and star formation history on optical colors can be separated. Galaxies with high dust attenuation follow the attenuation curve and are red in both $U - V$ and $V - J$ colors, whereas old stellar populations are relatively bluer in $V - J$ colors.



Original content from this work may be used under the terms of the [Creative Commons Attribution 4.0 licence](#). Any further distribution of this work must maintain attribution to the author(s) and the title of the work, journal citation and DOI.

The *UVJ* diagram (or other similar rest-frame color–color selections; e.g., Arnouts et al. 2013; Leja et al. 2019; Antwi-Danso et al. 2022) has become ubiquitous to distinguish between star-forming and quiescent galaxies (Brammer et al. 2009; Williams et al. 2009; Whitaker et al. 2011; Ilbert et al. 2013; Muzzin et al. 2013; Davidzon et al. 2017; Akins et al. 2022). While rest-frame color selections have been used when studying integrated galaxy properties, the comparably worse sensitivity and spatial resolution of Spitzer/IRAC (i.e., the only instrument able to image the rest-frame *J* band at $z \gtrsim 1$) has limited resolved studies of high-redshift galaxies.

The landscape of spatially resolved studies of high-redshift galaxies has changed with the recent launch and commissioning of the James Webb Space Telescope (JWST). With the combination of the longer-wavelength coverage and improved spatial resolution and sensitivity, JWST facilitates studying the spatially resolved rest-frame NIR emission of galaxies at $z \sim 2$. In this paper, we utilize early release observations from the Cosmic Evolution Early Release Science (CEERS; PI: Finkelstein; Finkelstein et al. 2017) to investigate this question: what is the physical cause of optical color gradients at $z \sim 2$? We construct resolved *UVJ* diagrams of galaxies from the 3D-HST catalog and study the radial gradients of galaxies within this plane. To model the light profiles, we use *imcascade*, a Bayesian implementation of the multi-Gaussian expansion (MGE) technique that provides a more flexible representation compared to traditional Sérsic profile fitting (Miller & van Dokkum 2021).

This paper is organized as follows. In Section 2, we describe the reduction of the JWST images, the *imcascade* modeling procedure, and the conversion from observed filters to rest-frame *UVJ* measurements. Section 3 displays our resolved *UVJ* measurements. The physical implications of our findings are discussed in Section 4. Throughout this study, we assume a flat Λ CDM cosmology with $H_0 = 70 \text{ km}^{-1} \text{ s}^{-1} \text{ Mpc}^{-1}$ and $\Omega_m = 0.3$. All radii are referred to along the semimajor axis. All magnitudes are reported on the AB system.

2. Methods

2.1. Data, Galaxy Sample, and *imcascade* Modeling

The NIRC*am* imaging used in this study was taken between 2022 June 22 and 28 as part of the CEERS survey (see Finkelstein et al. 2017, 2022) covering roughly 40 arcmin^2 in the AEGIS field. For this study, we focus on the three broadband filters: F115W, F200W, and F356W. Stage 2 calibrated data were used from the available MAST archive. Additional reduction, aligning, and coadding were performed with the *grizli* software package (Brammer 2019). Zero-points were used from the available calibration file `jwst_0942.pmap` with additional per-chip corrections in each band based on standard stars in the LMC.¹¹ This correction has been further verified to be accurate to $<0.04 \text{ mag}$ using data from M92, although there may be additional time variability (Boyer et al. 2022). All fitting was done on a common pixel scale of $0''.04 \text{ pixel}^{-1}$. Weight maps were also calculated using *grizli* with Poisson noise included.

To construct our galaxy sample, we begin with the 3D-HST catalog in the AEGIS field (Skelton et al. 2014; Momcheva et al. 2016) and select galaxies with $\log M_*/M_\odot > 10$ at

$1.7 < z < 2.3$ that lie within the footprint of the first epoch of CEERS data. Here z_{best} is used as the redshift measurement that corresponds to the spectroscopic, grism, or photometric redshift in this rank order, depending on what is available. The grism and the photometric redshifts are calculated using EAZY (Brammer et al. 2008). This creates an initial sample of 119 galaxies.

We fit the light distribution for galaxies in this sample in each of the three NIRC*am* bands using *imcascade* (Miller & van Dokkum 2021), a Bayesian implementation of the MGE technique that models galaxy light distribution as a mixture of Gaussians. This provides a more flexible representation compared to traditional parametric Sérsic fits, making it ideal for measuring complex color profiles. We briefly describe our procedure below but refer the reader to Miller & van Dokkum (2021) for a full description of the method and implementation.

To begin, we create cutouts of each galaxy in each band with a size $35 \times r_{\text{vdW}12}$ based on the F160W measured size from the van der Wel et al. (2012) catalog. Point-spread functions (PSFs) for each band are generated using *webbpsf* (Perrin et al. 2014), and the drizzled PSF was calculated using the same parameters used to create the mosaic. For use in *imcascade*, we fit the PSF in each band with an MGE model using five Gaussian components for F115W and F200W and four components for F356W. We use the same set of 10 Gaussian components to model each galaxy in every band, with widths logarithmically spaced from 0.75 pixels to $9 \times r_{\text{vdW}12}$. In each image, a three-parameter tilted plane sky model is simultaneously fit. Masks for nearby sources are created for each band separately using the segmentation tool in *photutils* (Bradley et al. 2020), specifically using a signal-to-noise threshold of 3 with a deblending threshold of 0.005. We expand this initial mask (where masked pixels have a value of 1) by convolving with a Gaussian of width 2.5 pixels and masking all pixels above 0.01.

Bayesian inference with *imcascade* is carried out with the nested sampling code *dynesty* (Speagle 2020) utilizing the “express” method, where the position, axis ratio, and position angle of the components are measured from least-squares fitting and kept constant while the posteriors of the fluxes of each component and the sky parameters are explored. This allows for much faster model creation, greatly speeding up execution time by a factor of roughly 100. The fluxes of each component are explored in logarithmic space using the informed priors discussed in Miller & van Dokkum (2021). Throughout the paper, we report colors integrated between annular bins, using the best-fit axis ratio and position angle, from the intrinsic (i.e., PSF deconvolved) *imcascade* models for each filter of each galaxy. For each measurement, we take 150 samples from the posterior distribution and report the median value with error bars representing the 16th–84th percentile range.

We perform a set of quality checks once inference is complete to select a high-quality sample for this study. In each filter, we ensure that none of the parameters in the optimized least-squares solution are at the bounds provided, a sign of an ill-converged fit and that the derived parameters are not robust. Additionally, we require the axis ratio to be $q > 0.1$ and the flux contained in the Gaussian component with the largest width to be less than 20% of the total flux, both signs of issues with background structure or unmasked sources. We find that 54 of the 119 galaxies pass all of the checks and will be used

¹¹ For more details on these corrections, see <https://github.com/gbrammer/grizli/pull/107>.

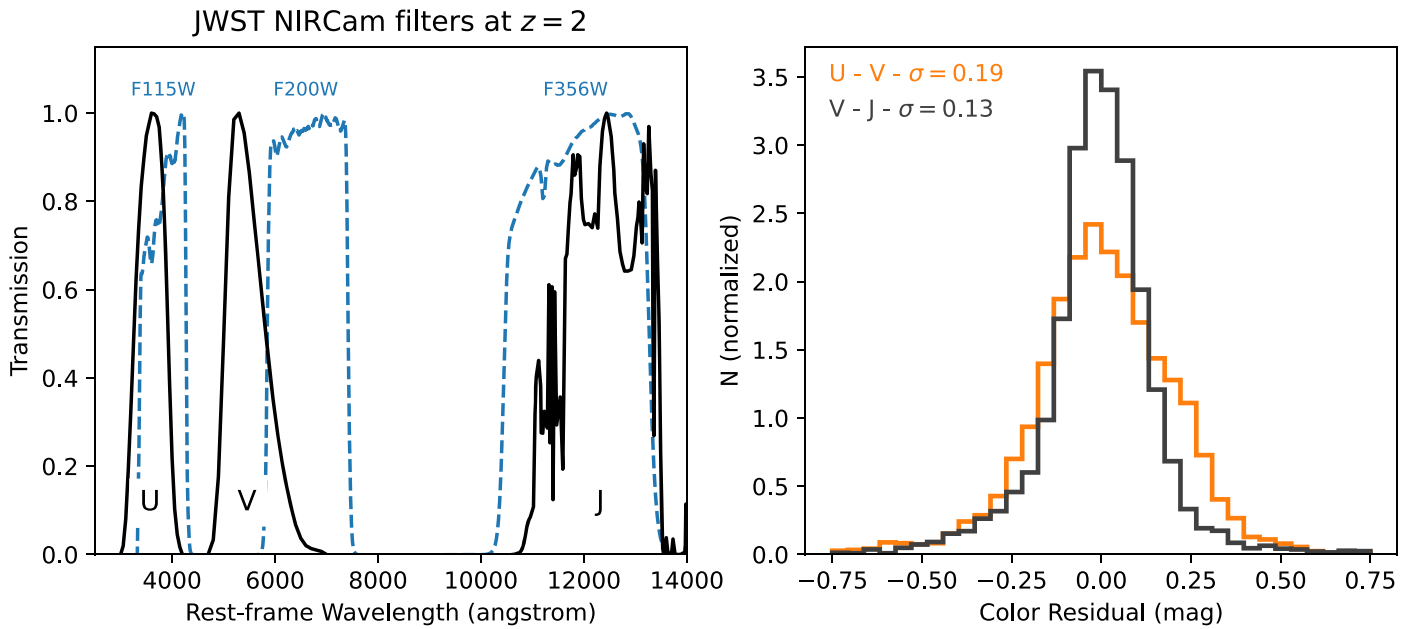


Figure 1. (Left) Filter transmission curves for rest-frame U , V , and J (black) along with JWST filters for a galaxy if observed at $z = 2$ (blue dashed). (Right) Residuals between true $U - V$ and $V - J$ colors and those calculated from observed JWST filters using Equation (1) for 10^4 simulated spectra with `prospector`. We find good agreement between the true and calculated rest-frame colors over the entire redshift range for all galaxy types.

for the remainder of the paper. The distributions of redshift, stellar mass, and specific star formation rate (sSFR) for the galaxies that did and did not pass these checks are similar. From visual inspection, we find that most of the galaxies that did not pass had issues with masking. Some were present in crowded fields where proper masking is difficult, while others had the target galaxy overmasked or nearby sources left unmasked.

2.2. Conversion to Rest-frame Filters

In order to ensure an accurate conversion between the observed and rest-frame colors, we use simulated spectra to fit a redshift-dependent relation. Figure 1 shows normalized filter transmission curves of rest-frame U , V , J compared to JWST NIRCcam filters for a galaxy observed at $z = 2$. For this study, we use F115W as a proxy for the rest-frame U band, F200W as a proxy for the rest-frame V band, and F356W for J . To ensure accurate conversion, we simulate 10^4 spectra for realistic galaxies at $z \sim 2$ using `PROSPECTOR` (Leja et al. 2017; Johnson et al. 2021). These galaxies are generated at $1.7 < z < 2.3$ using delayed- τ parametric star formation histories with an additional burst component and a contribution from nebular emission lines. The prior on the strength of the burst is a uniform 0%–50% of the total stars formed, and the age as a fraction of the age of the universe at $z \sim 2$ is uniform between 0.5 and 1. A fixed Calzetti et al. (2000) dust curve is used, and the optical depth in the V band is varied uniformly between zero and 3. From these simulated spectra, we can calculate the observed flux in the JWST NIRCcam filters and compare directly with the rest-frame U -, V -, and J -band fluxes. We fit a linear relation between the observed colors and the known rest-frame colors along with a linear redshift evolution term. The form of this equation, along with the best-fit values

for each color, is as follows:

$$(U - V)_{\text{RF}} = 0.971 (m_{115\text{W}} - m_{200\text{W}}) + 0.056 - 0.969 (z - 2), \quad (1)$$

$$(V - J)_{\text{RF}} = 1.310 (m_{200\text{W}} - m_{356\text{W}}) + 0.168 - 0.268 (z - 2). \quad (2)$$

These relations are valid only across the redshift range of $1.7 < z < 2.3$. At $z < 1.7$, F115W shifts redward of the rest-frame U band, introducing systematic errors due to extrapolation. At $z > 2.3$, F356W becomes too “blue” and no longer overlaps with rest-frame J , similarly complicating the conversion. The residuals between the true and calculated UVJ colors for the simulated galaxies are shown in Figure 1. The standard deviation of the residuals, $\sigma = 0.19$ mag for $U - V$ and $\sigma = 0.13$ for $V - J$, is consistent across all galaxy types and relatively small compared to the 2 mag range that galaxies span in each color. This scatter is consistent with redshift for the $V - J$ conversion but increases slightly at lower redshifts for $U - V$. While typical redshift uncertainties ($\sigma_z \lesssim 0.05$) will not increase this scatter significantly, catastrophic errors in the redshifts of individual galaxies will lead to outliers in rest-frame color space. This is only expected for roughly 3% of galaxies in the AEGIS field (Skelton et al. 2014; Bezanson et al. 2016). We follow previous studies and use a simple relation to convert to rest-frame colors because we are only using three filters (Wang et al. 2017). However, there are methods, such as EAZY (Brammer et al. 2008), that use physically motivated templates for the galaxy’s spectral energy distribution (SED) that should lead to a more accurate conversion. To test if there is any benefit, we apply EAZY to calculate the rest-frame colors from the `PROSPECTOR` mock photometry using the same three filters. We find very similar

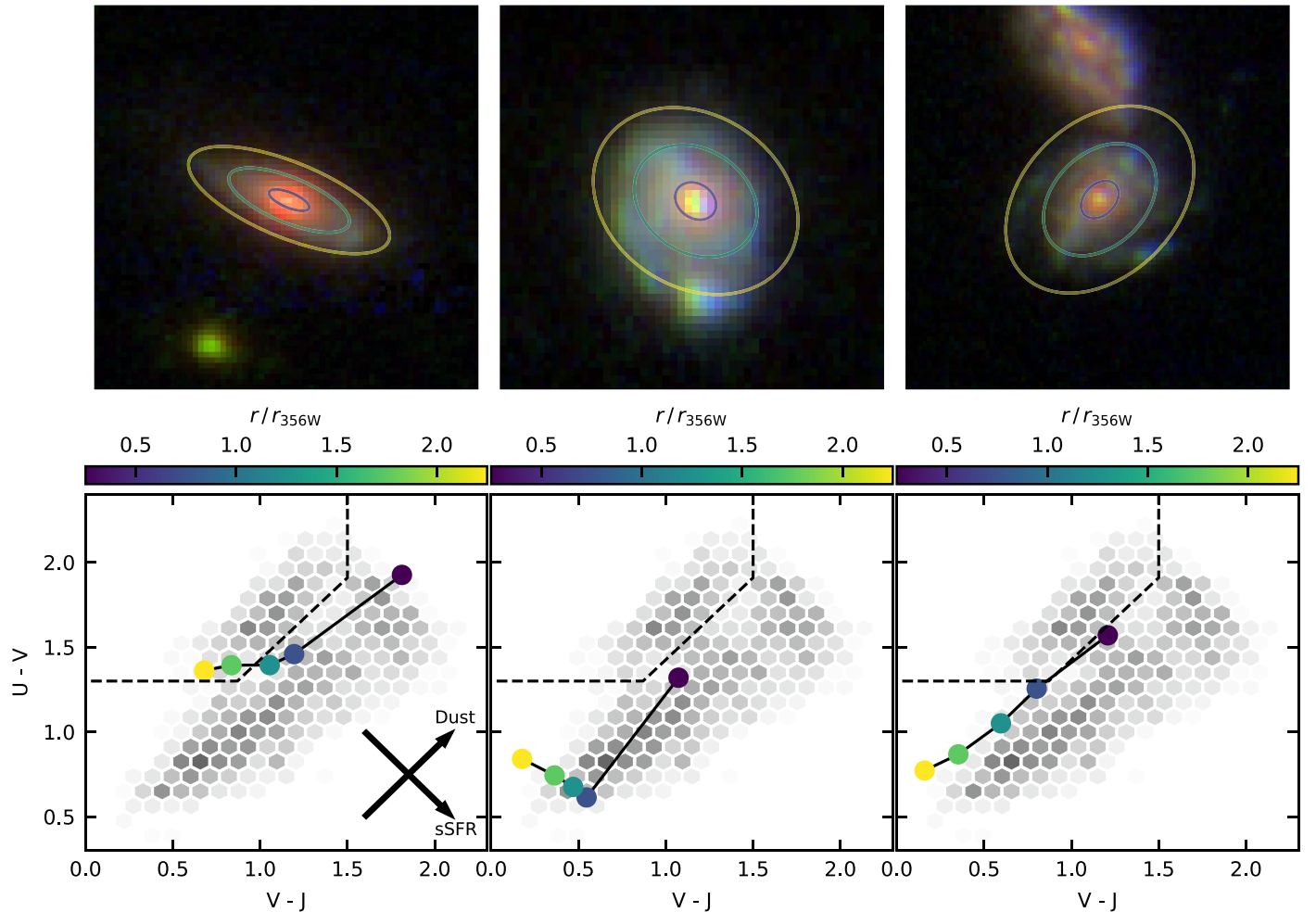


Figure 2. The RGB images (F356W, F200W, and F150W filters) of three example galaxies (top) and their corresponding resolved UVJ diagrams (bottom). The colored track indicates the evolution in rest-frame color from the innermost region (purple) to the outskirts at $>2r_e$ (yellow). These colors are mirrored on the RGB images to show the corresponding radii. The dotted line shows the cutoff between star-forming and quiescent from Muzzin et al. (2013), and the gray histogram in the background shows the distribution of galaxies in the same mass and redshift range from 3D-HST. Vectors illustrating the expected effect of increasing dust and sSFR are indicated in the bottom right corner.

accuracy to the linear relations used here; the standard deviations of the EAZY residuals are 0.21 mag for $U - V$ and 0.12 for $V - J$, compared to 0.19 and 0.13, respectively, for the linear relations. While this is not a perfect comparison, as EAZY and PROSPECTOR make different assumptions about the physical properties of galaxies, it is indicative that the template-based methods provide little benefit over the simple linear relation when a small number of filters are used.

As a check on our procedure, we compare our rest-frame color measurements to those in the 3D-HST catalog. We integrate our `imcascade` models convolved with the PSF to a radius of $0''.35$, similar to the apertures used in the 3D-HST catalog (Skelton et al. 2014). We find good agreement, with a mean difference of less than 0.05 mag and a scatter of 0.23 mag for both colors.

3. Results

Figure 2 presents RGB renderings showing F356W, F200W, and F150W images of three example galaxies. We construct resolved UVJ diagrams by calculating the integrated colors with bins of width $0.5r_{F356W}$ from the center out to $2.5r_{F356W}$. The colors of each point denote the average radii used to

calculate the UVJ colors and correspond to the ellipses plotted on the RGB images. These measurements are shown alongside the distribution of integrated UVJ colors from galaxies over the same mass and redshift range from the 3D-HST survey. The three galaxies chosen are all at $z \sim 1.8$ and show a variety of UVJ color profiles.

To help build intuition, we show illustrative arrows indicating how we expect the sSFR and dust to vary across the UVJ plane. The effect of dust follows a vector in this plane set by the attenuation curve. A Calzetti et al. (2000)-like dust curve is often used, but there is known to be some variation in the attenuation curves of galaxies at high redshift (Kriek & Conroy 2013; Reddy et al. 2015). Following this relation, dust attenuation increases from bottom left to top right. The sSFR is observed to vary in the orthogonal direction, decreasing from bottom right to top left (Wang et al. 2017). Quiescent galaxies are commonly chosen as being above the selection line shown in Figure 2 (Muzzin et al. 2013). In essence, this is selecting for the presence of a strong Balmer break, indicative of an old stellar population. Within this quiescent region, there is also known to be an age sequence (Whitaker et al. 2012, 2013; Belli et al. 2019). We discuss the interpretation of quiescent galaxies further in Section 3.2. We refer the reader to Leja et al. (2019)

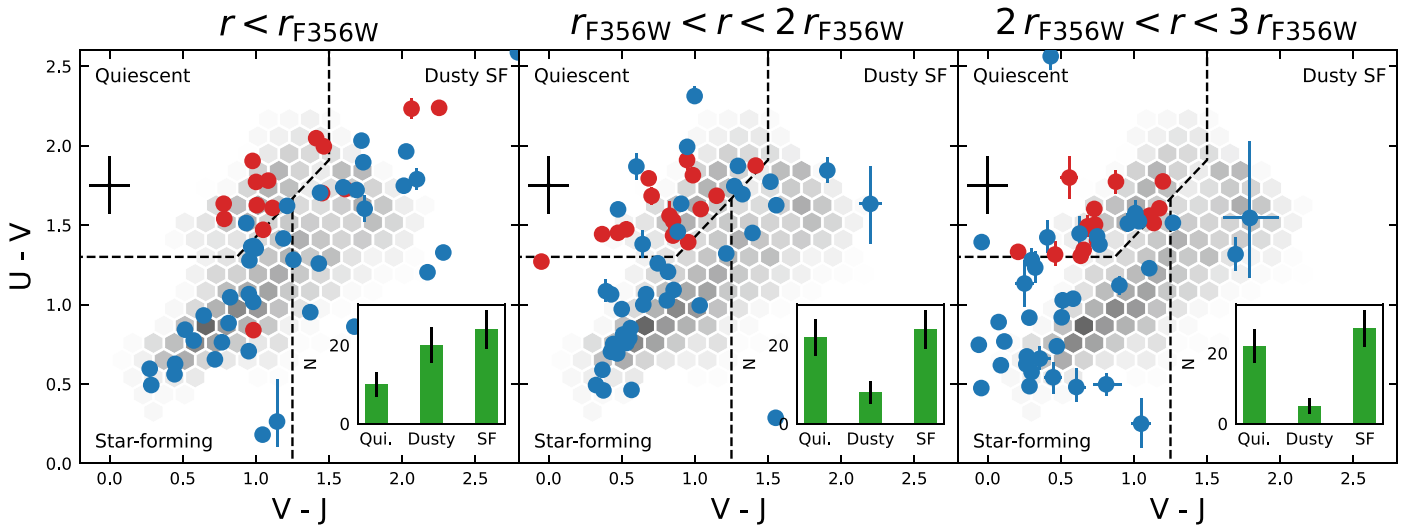


Figure 3. The UVJ colors for individual galaxies measured within three separate radial bins. The dotted line shows the cutoff between star-forming and quiescent from Muzzin et al. (2013), and the gray histogram in the background shows the distribution of galaxies in the same mass and redshift range from 3D-HST. Galaxies are separated into star-forming (blue) and quiescent (red) based on their total $U - V$ and $V - J$ colors measured with *imcascade*. Observational uncertainties are shown as error bars on individual points, and the black error bar in the top left shows the additional uncertainty due to converting from observed to rest-frame colors. We classify each region of each galaxy into quiescent, star-forming, or dusty star-forming (see text for more details), and the inset bar graphs show the distribution of each classification at each radius.

for a more in-depth discussion of how galaxy properties vary across the UVJ plane.

The three galaxies shown all display disk morphology with a red center. The galaxies on the left and right are bluer in $U - V$ and $V - J$ at larger radii, consistent with radially decreasing dust attenuation (Nelson et al. 2016; Liu et al. 2017). The galaxy on the left appears to be edge-on and has much higher dust attenuation overall (e.g., Nelson et al. 2022). The galaxy in the middle also shows high central dust attenuation but a positive $U - V$ gradient at $r > r_{F356W}$. This implies a higher sSFR in the outskirts. These images display the ability of JWST to study the resolved structure of galaxies at cosmic noon along with the complex galaxy structure already in place at the epoch. Comparison of the UVJ gradients highlights the need for subarcsecond rest-frame NIR observations to untangle the spatially complex dust and stellar populations of $z \sim 2$ galaxies.

Figure 3 displays a resolved view of the UVJ color-color plane for the galaxies in our sample. The three panels show UVJ colors measured from the intrinsic *imcascade* models integrated in the ranges $0 < r < r_{F356W}$, $r_{F356W} < r < 2r_{F356W}$, and $2r_{F356W} < r < 3r_{F356W}$ from left to right. At small radii, we find some star-forming galaxies with very strong dust attenuation ($U - V \gtrsim 1.5$, $V - J \gtrsim 1.5$), but this population largely disappears when looking at the outskirts of galaxies. The entire population of star-forming galaxies appears to shift toward the bottom left of the color-color plane, i.e., predominantly unobscured star formation. The behavior and interpretation of quiescent galaxies in this plane is more complex and is discussed further in Section 3.2. To help understand the physical causes of these color gradients, we classify each radial bin of each galaxy as quiescent, dusty star-forming, or star-forming. The quiescent selection follows Muzzin et al. (2013). We then classify each radial bin of each galaxy as dusty star-forming if $V - J > 1.25$ and as star-forming if not. We note that this classification may not be intrinsic and is impacted by viewing angle and dust geometry (Patel et al. 2012; Zuckerman et al. 2021). These regions are

labeled in Figure 3, and the inset bar graphs display the distribution of classifications at each radius.

We find that the number of galaxies classified as star-forming remains constant in all three radius bins. The number of galaxies classified as dusty star-forming is high in the inner regions but drops significantly in the outer regions. Correspondingly, when looking at the inner regions, there are only 10 galaxies classified as quiescent in their inner region, which rises to 22 at $2r_{F356W} < r < 3r_{F356W}$. In this largest radius bin, there are a number of galaxies that have UVJ colors near the cutoff between star-forming and quiescent with $U - V \lesssim 1.5$ and $V - J < 1$.

3.1. UVJ Gradients in Star-forming Galaxies

In this section, we focus on the UVJ gradients of star-forming galaxies. They make up roughly 75% of our sample (39/54), and the physical interpretation of the UVJ plane is well established. Figure 4 displays the differences between $U - V$ and $V - J$ color between the outer galaxy, which we define as $2r_{\text{eff},F356W} < r < 3r_{\text{eff},F356W}$, and the inner galaxy, defined as $r < r_{\text{eff},F356W}$. Figure 4 visualizes examples from the four quadrants of the $\Delta(U - V) - \Delta(V - J)$ plane and how these gradients would appear in the UVJ color-color plane along with the presumed physical cause of the gradient. We focus on the effects of dust and sSFR, which have orthogonal effects in the UVJ plane. In real galaxies, there are likely multiple effects that could cause color gradients, yet these quadrants are a useful tool to understand the dominant physical processes that affect galaxies.

The largest fraction of star-forming galaxies lies in quadrant three of this plane, corresponding to negative $U - V$ and $V - J$ gradients. The color gradients of these galaxies are consistent with differential dust attenuation, with higher dust content in the center compared to the outskirts. In contrast, only 8% of galaxies in our sample reside in Q1, where we expect the dust attenuation to be higher in the outskirts. A smaller fraction of galaxies reside in either Q2 or Q4. These gradients are consistent with the following radial variation in stellar

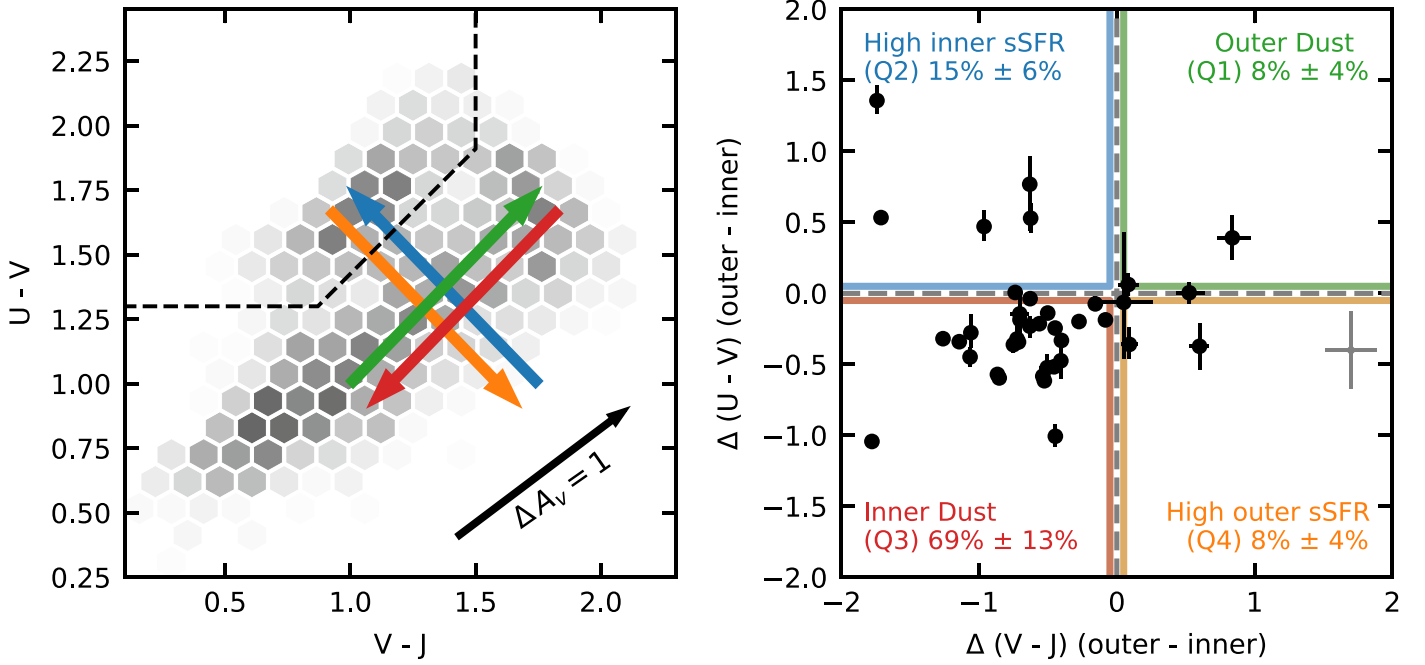


Figure 4. The UVJ gradients of star-forming galaxies. (Right) The change in the $U - V$ and $V - J$ colors from the outer ($2r_{356W} < r < 3r_{356W}$) to the inner ($r < r_{356W}$) galaxy is shown. As with the figure above, observational uncertainties are shown with individual data points, and the additional uncertainty due to converting from observed to rest-frame fits is shown as in the gray error bar on the right. We highlight the fraction of galaxies in our sample that reside in each quadrant, along with the physical interpretation. These colors correspond to the arrows in the left panel. (Left) Examples of gradients in the UVJ plane corresponding to the four quadrants in the right panel. The arrows signify the movement from inner to outer radii moving from the base to the head of the arrow.

populations: high sSFR or younger age in the central region in Q2 or the outskirts for Q4. Galaxies exhibiting a classical old bulge and star-forming disk, like the Milky Way, would likely live somewhere in Q4. These galaxies tend to have a relatively high sSFR ($\log \text{sSFR} \sim -9 \text{ yr}^{-1}$). To isolate the effects of dust and sSFR in Figure 5, we show the change in S_{SED} and C_{SED} colors, defined in Fang et al. (2018). This is a 34.8° rotation of the UVJ axis such that it is parallel with the star-forming sequence. The S_{SED} measures the net slope of the SED that is correlated with dust content, while C_{SED} quantifies the curvature and is correlated with sSFR; see Fang et al. (2018) for more details. For many of the galaxies in Q3, ΔC_{SED} is consistent with zero, implying that radially decreasing dust attenuation is the sole cause of the color gradients. There does appear to be a slight bias to the positive ΔC_{SED} values, which would imply the additional effect of increased central star formation. The implied median change in dust attenuation for galaxies in Q3 is $\Delta A_V = -0.86$ between the outer and inner regions with a standard deviation of $0.45 \Delta A_V$, which does not correlate strongly with galaxy properties or redshift.

3.2. UVJ Gradients in Quiescent Galaxies

Our discussion so far has focused on star-forming galaxies, as they make up the majority of our sample, and the physical interpretation is relatively straightforward, as described above. The interpretation of quiescent galaxies becomes more complicated, as there is known to be an age gradient along this sequence that displays a similar vector to differential dust attenuation (Whitaker et al. 2012; Belli et al. 2019). Figure 6 displays the Calzetti dust vector along with the age sequence measured from Belli et al. (2019). These two are almost parallel, complicating the interpretation of $\Delta(U - V)$ and Δ

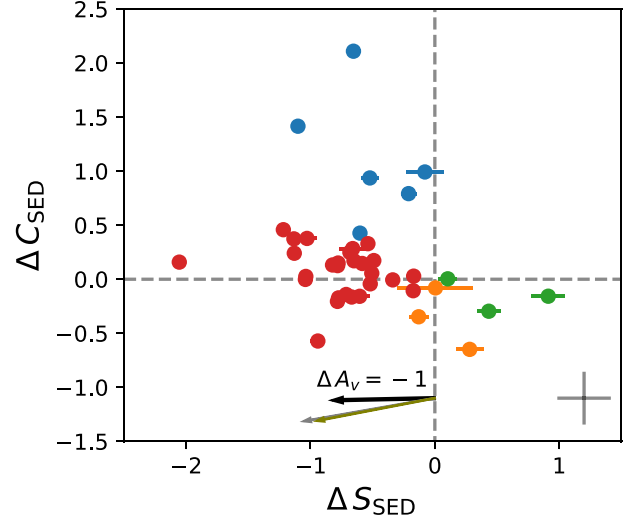


Figure 5. Gradients in S_{SED} and C_{SED} colors, a rotated version of the UVJ color-color space proposed in Fang et al. (2018). The horizontal axis shows ΔS_{SED} , which is correlated with dust content, and the vertical axis shows ΔC_{SED} , which is correlated with star formation. Negative values on the horizontal axis imply higher dust attenuation in the centers of galaxies. The colors of the points represent which quadrant they inhabit in Figure 4. The black arrow displays the change in color corresponding to $\Delta A_V = -1$ according to the Calzetti et al. (2000) dust curve. The olive and gray arrows show this using Reddy et al. (2015) and Salmon et al. (2016; moving from $A_V = 1 \rightarrow 0$), respectively. Many of the galaxies in Q3 (red points) are consistent with $\Delta C_{\text{SED}} = 0$, implying that radial decreasing dust attenuation is the sole cause of color gradients.

$(V - J)$ as the galaxy's location in UVJ space becomes important.

Quiescent galaxies in our sample show a range of UVJ gradients. Six of the 15 galaxies are classified as star-forming in

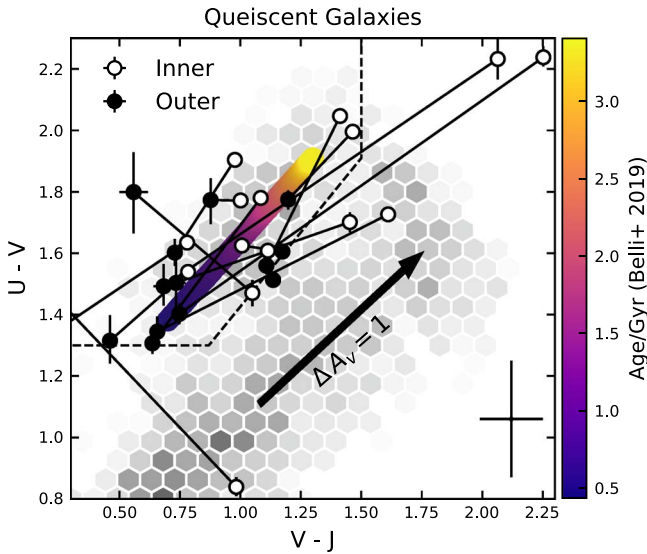


Figure 6. The UVJ colors of quiescent galaxies, comparing their inner ($r < r_{356W}$) and outer ($2r_{356W} < 3r_{356W}$) regions. Galaxies are categorized using their integrated UVJ colors following Muzzin et al. (2013). The empirical age gradient derived in Belli et al. (2019) is shown along with the Calzetti et al. (2000) dust vector. There is a diversity of UVJ gradients within quiescent galaxies, but we note that for roughly one-third of our sample (6 of 15), the inner region lies within the star-forming section of the UVJ plane.

their inner region and within the UVJ quiescent region in their outskirts. Two of these galaxies have very red centers, $U - V > 2$ and $V - J > 2$, suggesting high dust attenuation; these galaxies are both quite compact, and we do not show any morphological signs of dust. This is similar to the behavior of star-forming galaxies in Q2 displayed in Figure 4. Another four of the galaxies show relatively mild UVJ gradients within the quiescent region ($\Delta(U - V)$ and $\Delta(V - J) < 0.3$). The final five galaxies show gradients within the quiescent region that are parallel to the age sequence derived in Belli et al. (2019) or with radially decreasing dust attenuation.

4. Discussion and Summary

In this study, we have used early science observations from JWST NIRCcam to investigate color gradients within galaxies at $z \sim 2$. Specifically, we are interested in this question: what is the underlying cause of color gradients at cosmic noon? Previously, with only rest-frame optical colors at subarcsecond resolution, there was no way to definitively answer this question. We use data taken as part of the CEERS survey in the well-studied AEGIS field and construct a sample of galaxies above $\log M_*/M_\odot > 10$ at $1.7 < z < 2.3$ from the 3D-HST catalog. We model the light distribution for our sample of galaxies in three NIRCcam bands with *imcascade*, a Bayesian implementation of the MGE technique that flexibly models galaxy profiles as a mixture of Gaussians. This technique is well suited for measuring complex galaxy profiles in high signal-to-noise ratio data, like those in JWST images, as shown in Figure 2. From the *imcascade* models, we calculate resolved $U - V$ and $V - J$ colors based on the $m_{F115W} - m_{200W}$ and $m_{200W} - m_{F356W}$ colors, respectively.

For star-forming galaxies, we observe that the large majority of galaxies, roughly 70%, show UVJ gradients consistent with strong central dust attenuation ($A_V > 1$). Radial dust attenuation gradients have been observed at $z \lesssim 1.5$. Wang et al. (2017) studied stacked UVI (similar to the UVJ plane) gradients in

star-forming galaxies out to $z = 1.5$ and concluded that dust is the main cause of color gradients. Liu et al. (2016) inferred that dust is the main cause of NUV-B gradients in $0.5 < z < 1.5$. Nelson et al. (2016) studied resolved Balmer decrements and found that the attenuation of the H_α line can increase by up to 2 mag in the center of massive galaxies. It has also been suggested that dust gradients continue to play a large role in galaxies at $z > 1.5$ using lower-wavelength HST data (Liu et al. 2017; Miller et al. 2022). This study provides the first definitive evidence confirming that dust is the cause of negative color gradients out to $z = 2.3$. Given that the ratios of far-IR and millimeter sizes continue to be smaller than optical sizes out to $z \sim 4$ (Fujimoto et al. 2017; Tadaki et al. 2020), we suspect that dust gradients will still play a large role in shaping color gradients and observed morphologies in galaxies at higher redshift. Numerical simulations suggest that even at $z > 6$, dust continues to play a large role in shaping the rest-frame optical and UV morphology of galaxies (Marshall et al. 2022).

It is worth highlighting that this result is qualitatively different from what is observed in spiral galaxies in the local universe. Galaxies like Andromeda or the Milky Way also show negative color gradients; however, they are caused by an old, mostly dust-free bulge and a younger star-forming disk (de Jong 1996). This would manifest as a UVJ gradient in quadrant four (orange in Figure 4), in which only a small fraction of our sample resides. Our observations are consistent with the scenario of dust-obscured bulge growth at high redshift (Tacchella et al. 2018; Nelson et al. 2019). It is possible that there are also sSFR/age gradients in our sample that are simply being “outshone” by the dominant gradient in dust opacity. Resolved SED modeling would be required to further investigate simultaneous gradients of multiple physical properties. Metallicity gradients are also thought to play a large role in local galaxies (e.g., Tortora et al. 2011). There is no clear signature of metallicity in the UVJ plane. Again, detailed SED modeling or resolved spectroscopy is needed to investigate metallicity gradients.

We find that a substantial fraction of our star-forming galaxies (23%) have UVJ gradients consistent with gradients in stellar population properties, mainly sSFR. These gradients are orthogonal to the dust vector in the UVJ plane. Roughly two-thirds of these galaxies show a central star formation burst, while the other one-third show stronger star formation in the outskirts. This is combined with a similar population of quiescent galaxies whose inner regions reside in the star-forming region of UVJ space. While they are a smaller fraction of the total population of star-forming galaxies, they likely represent important transitional phases in their formation history. Those with central star formation could be related to the growth of bulges observed in local spiral galaxies (Nelson et al. 2018; Tadaki et al. 2020). The galaxies with outer star formation could be in the process of inside-out quenching (e.g., Spilker et al. 2019; Akhshik et al. 2022). Further studies of these transitional galaxies will help illuminate quenching mechanisms at cosmic noon.

Interpreting UVJ gradients in quiescent galaxies is more complicated. We see some galaxies with color gradients consistent with the known age gradient along the quiescent sequence (Whitaker et al. 2012; Belli et al. 2019); however, this is almost parallel to the effect of radially decreasing dust. Other studies have found that UVJ colors alone cannot constrain the

age of a stellar population, suggesting instead that observed correlations between *UVJ* colors and age arise from secondary correlations or scaling relationships with other parameters (Leja et al. 2019). Resolved spectroscopy or mid-IR/far-IR measurements could help differentiate between the effects of dust and stellar age. The globally quiescent galaxies with ongoing star formation in their centers may represent an early stage of quenching or experiencing a rejuvenation event (e.g., Akhshik et al. 2021). The presence of quiescent galaxies without strong color gradients provides a clue that there are multiple quenching pathways (Woo & Ellison 2019; Suess et al. 2021; Akhshik et al. 2022). A larger sample and more detailed modeling is need to fully understand color gradients in early quiescent galaxies.

This study represents the very beginning of how JWST will unveil the resolved structure of galaxies at cosmic noon. With rest-frame NIR imaging at the resolution of JWST, we will be able to investigate gradients in stellar age, dust, and other physical properties at the peak epoch of galaxy growth. The JWST opens the window to a more complete and detailed view of how galaxies form and evolve in the early universe.

T.B.M. would like to thank Patricia Gruber and the Gruber Foundation for their support of the work presented here. Cloud-based data processing and file storage for this work is provided by the AWS Cloud Credits for Research program.

Some of the data presented in this paper were obtained from the Mikulski Archive for Space Telescopes (MAST) at the Space Telescope Science Institute. The specific observations analyzed can be accessed via [10.17909/2hft-5f48](https://doi.org/10.17909/2hft-5f48).

ORCID iDs

Tim B. Miller  <https://orcid.org/0000-0001-8367-6265>
 Katherine E. Whitaker  <https://orcid.org/0000-0001-7160-3632>
 Erica J. Nelson  <https://orcid.org/0000-0002-7524-374X>
 Pieter van Dokkum  <https://orcid.org/0000-0002-8282-9888>
 Rachel Bezanson  <https://orcid.org/0000-0001-5063-8254>
 Gabriel Brammer  <https://orcid.org/0000-0003-2680-005X>
 Kasper E. Heintz  <https://orcid.org/0000-0002-9389-7413>
 Joel Leja  <https://orcid.org/0000-0001-6755-1315>
 Katherine A. Suess  <https://orcid.org/0000-0002-1714-1905>
 John R. Weaver  <https://orcid.org/0000-0003-1614-196X>

References

- Akhshik, M., Whitaker, K. E., Leja, J., et al. 2021, *ApJL*, 907, L8
 Akhshik, M., Whitaker, K. E., Leja, J., et al. 2022, arXiv:2203.04979
 Akins, H. B., Narayanan, D., Whitaker, K. E., et al. 2022, *ApJ*, 929, 94
 Antwi-Danso, J., Papovich, C., Leja, J., et al. 2022, arXiv:2207.07170
 Arnouts, S., Le Floc'h, E., Chevillard, J., et al. 2013, *A&A*, 558, A67
 Belli, S., Newman, A. B., & Ellis, R. S. 2019, *ApJ*, 874, 17
 Bezanson, R., Wake, D. A., Brammer, G. B., et al. 2016, *ApJ*, 822, 30
 Boyer, M. L., Anderson, J., Gennaro, M., et al. 2022, *RNAAS*, 6, 191
 Bradley, L., Sipőcz, B., Robitaille, T., et al. 2020, astropy/photutils: v1.0.0, Zenodo, doi:10.5281/zenodo.4044744
 Brammer, G. 2019, Grism redshift and line analysis software, Astrophysics Source Code Library, ascl:1905.001
 Brammer, G. B., van Dokkum, P. G., & Coppi, P. 2008, *ApJ*, 686, 1503
 Brammer, G. B., Whitaker, K. E., van Dokkum, P. G., et al. 2009, *ApJL*, 706, L173
 Calzetti, D., Armus, L., Bohlin, R. C., et al. 2000, *ApJ*, 533, 682
 Chan, J. C. C., Beifiori, A., Mendel, J. T., et al. 2016, *MNRAS*, 458, 3181
 Davidzon, I., Ilbert, O., Laigle, C., et al. 2017, *A&A*, 605, A70
 de Jong, R. S. 1996, *A&A*, 313, 377
 Fang, J. J., Faber, S. M., Koo, D. C., et al. 2018, *ApJ*, 858, 100
 Finkelstein, S. L., Bagley, M. B., Arrabal Haro, P., et al. 2022, *ApJL*, 940, L55
 Finkelstein, S. L., Dickinson, M., Ferguson, H. C., et al. 2017, The Cosmic Evolution Early Release Science (CEERS) Survey, JWST Proposal ID 1345. Cycle 0 Early Release Science
 Franx, M., & Illingworth, G. 1990, *ApJL*, 359, L41
 Fujimoto, S., Ouchi, M., Shibuya, T., & Nagai, H. 2017, *ApJ*, 850, 83
 Ilbert, O., McCracken, H. J., Le Fèvre, O., et al. 2013, *A&A*, 556, A55
 Johnson, B. D., Leja, J., Conroy, C., & Speagle, J. S. 2021, *ApJS*, 254, 22
 Kormendy, J., & Djorgovski, S. 1989, *ARA&A*, 27, 235
 Kriek, M., & Conroy, C. 2013, *ApJL*, 775, L16
 La Barbera, F., & de Carvalho, R. R. 2009, *ApJL*, 699, L76
 Labbé, I., Huang, J., Franx, M., et al. 2005, *ApJL*, 624, L81
 Leja, J., Johnson, B. D., Conroy, C., van Dokkum, P. G., & Byler, N. 2017, *ApJ*, 837, 170
 Leja, J., Tacchella, S., & Conroy, C. 2019, *ApJL*, 880, L9
 Liu, F. S., Jiang, D., Faber, S. M., et al. 2017, *ApJL*, 844, L2
 Liu, F. S., Jiang, D., Guo, Y., et al. 2016, *ApJL*, 822, L25
 Marshall, M. A., Wilkins, S., Di Matteo, T., et al. 2022, *MNRAS*, 511, 5475
 Miller, T. B., & van Dokkum, P. 2021, *ApJ*, 923, 124
 Miller, T. B., van Dokkum, P., & Mowla, L. 2022, arXiv:2207.05895
 Momcheva, I. G., Brammer, G. B., van Dokkum, P. G., et al. 2016, *ApJS*, 225, 27
 Mosleh, M., Hosseinejad, S., Hosseini-ShahiSavandi, S. Z., & Tacchella, S. 2020, *ApJ*, 905, 170
 Muzzin, A., Marchesini, D., Stefanon, M., et al. 2013, *ApJ*, 777, 18
 Nelson, D., Pillepich, A., Springel, V., et al. 2018, *MNRAS*, 475, 624
 Nelson, E. J., Suess, K. A., Bezanson, R., et al. 2022, arXiv:2208.01630
 Nelson, E. J., Tadaki, K.-i., Tacconi, L. J., et al. 2019, *ApJ*, 870, 130
 Nelson, E. J., van Dokkum, P. G., Förster Schreiber, N. M., et al. 2016, *ApJ*, 828, 27
 Patel, S. G., Holden, B. P., Kelson, D. D., et al. 2012, *ApJL*, 748, L27
 Perrin, M. D., Sivaramakrishnan, A., Lajoie, C.-P., et al. 2014, *Proc. SPIE*, 9143, 91433X
 Reddy, N. A., Kriek, M., Shapley, A. E., et al. 2015, *ApJ*, 806, 259
 Salmon, B., Papovich, C., Long, J., et al. 2016, *ApJ*, 827, 20
 Skelton, R. E., Whitaker, K. E., Momcheva, I. G., et al. 2014, *ApJS*, 214, 24
 Speagle, J. S. 2020, *MNRAS*, 493, 3132
 Spilker, J. S., Bezanson, R., Weiner, B. J., Whitaker, K. E., & Williams, C. C. 2019, *ApJ*, 883, 81
 Suess, K. A., Kriek, M., Price, S. H., & Barro, G. 2019, *ApJ*, 877, 103
 Suess, K. A., Kriek, M., Price, S. H., & Barro, G. 2021, *ApJ*, 915, 87
 Szomoru, D., Franx, M., van Dokkum, P. G., et al. 2013, *ApJ*, 763, 73
 Tacchella, S., Carollo, C. M., Schreiber, N. F., et al. 2018, *ApJ*, 859, 56
 Tadaki, K.-i., Belli, S., Burkert, A., et al. 2020, *ApJ*, 901, 74
 Tortora, C., Napolitano, N. R., Romanowsky, A. J., et al. 2011, *MNRAS*, 418, 1557
 van der Wel, A., Bell, E. F., Häussler, B., et al. 2012, *ApJS*, 203, 24
 Wang, W., Faber, S. M., Liu, F. S., et al. 2017, *MNRAS*, 469, 4063
 Whitaker, K. E., Kriek, M., van Dokkum, P. G., et al. 2012, *ApJ*, 745, 179
 Whitaker, K. E., Labbé, I., van Dokkum, P. G., et al. 2011, *ApJ*, 735, 86
 Whitaker, K. E., van Dokkum, P. G., Brammer, G., et al. 2013, *ApJL*, 770, L39
 Williams, R. J., Quadri, R. F., Franx, M., van Dokkum, P., & Labbé, I. 2009, *ApJ*, 691, 1879
 Woo, J., & Ellison, S. L. 2019, *MNRAS*, 487, 1927
 Wu, H., Shao, Z., Mo, H. J., Xia, X., & Deng, Z. 2005, *ApJ*, 622, 244
 Wuyts, S., Förster Schreiber, N. M., Genzel, R., et al. 2012, *ApJ*, 753, 114
 Wuyts, S., Labbé, I., Franx, M., et al. 2007, *ApJ*, 655, 51
 Zuckerman, L. D., Belli, S., Leja, J., & Tacchella, S. 2021, *ApJL*, 922, L32